LAWRENCE
LIVERMORE
NATIONAL
LABORATORY

LLNL-JRNL-645168

Rapidly Soldidified U-6wt%Nb Powders for Dispersion-Type Nuclear Fuels

J. T. McKeown, L. L. Hsiung, H. J. Ryu, J. M. Park, P. E. A. Turchi, W. E. King

October 25, 2013

Journal of Nuclear Materials

Disclaimer

LLNL-JRNL-645168

Rapidly Solidified U-6wt%Nb Powders for Dispersion-Type Nuclear Fuels

Joseph T. McKeown[1,*], Luke L. Hsiung[1], Ho Jin Ryu[2], Jong Man Park[3], Patrice E.A. Turchi[1], and Wayne E. King[1]

[1] Physical and Life Sciences Directorate, Lawrence Livermore National Laboratory, Livermore, CA 94550 USA

[2] Korea Advanced Institute of Science and Technology, Daejeon 305-701, Republic of Korea

[3] Korea Atomic Energy Research Institute, Daejeon 305-353, Republic of Korea

Abstract

The microstructures of U-6wt%Nb powder particles were investigated to assess their use as a distributed fuel phase in dispersion-type nuclear fuels. The powder was produced by centrifugal atomization, leading to rapid solidification of the molten alloy particles. The microstructure of the solidified particles consisted of a dendritic structure comprising metastable α-phase-related dendrites and interdendritic metastable γ^0 phase formation. The relationship between the observed microstructure and processing conditions are discussed, and the implications of the microstructure on the desired properties for dispersion-type nuclear fuel applications are evaluated.

[*] Corresponding author: Tel.: +1-925-422-1708; mckeown3@llnl.gov

1. Introduction

Dispersion-type nuclear fuels [1-8] offer numerous advantages for future-generation advanced nuclear fuel forms, such as high burn-up and irradiation resistance [3]. In particular, dispersed metallic inert matrix fuels (IMF) that employ uranium-alloy fuel kernels can provide a high tolerance for fission gases and irradiation dose while maintaining high fuel density and thermal conductivity [3-6]. Irradiation-induced structural and property changes can be minimized through localization of fission damage to specific, controlled regions within the fuel system. Porous regions in the fuel design allow for accommodation of gases, and a direct metallurgical bond between the fuel and cladding provides thermal conductivity and protects against fuel-cladding interactions.

While a dispersed metallic uranium fuel can provide a large quantity of fissile material per unit volume, a requirement for low-enriched uranium (LEU) fuels, the disadvantages of unalloyed uranium [9-13] preclude its use. The relatively low strength, low ductility, and poor oxidation and corrosion resistance of unalloyed uranium are detrimental to utilization of the metal, particularly under the conditions experienced in a reactor fuel, where enhanced corrosion properties and dimensional stability are necessary during thermal cycling and irradiation. These mechanical and corrosion properties are typically improved by the addition of alloying elements [9,12], most commonly with additions of early transition metals [14]. Uranium is often alloyed with niobium to increase oxidation and corrosion resistance, which can be accompanied by significant improvements to mechanical properties. For example, U-6wt%Nb alloys can have corrosion rates orders of magnitude lower than unalloyed uranium, combined with significant enhancements in the yield strength or tensile elongation relative to unalloyed uranium [13].

The resulting property enhancements due to alloying with niobium are dependent on crystal structure and niobium distribution, which in turn has a strong dependence on the cooling rate from high temperatures during processing. Under equilibrium conditions, reference to the uranium-niobium phase diagram [15] shows that niobium is extensively soluble in the high-temperature body-centered cubic (bcc) γ solid solution but essentially insoluble in the low-temperature orthorhombic α phase. U-6wt%Nb alloys have been found to possess the greatest corrosion resistance and mechanical properties when quenched at high enough rates to suppress diffusional decomposition of the high-

temperature γ phase and obtain the metastable martensitic α″ phase, due to uniform distribution of niobium in the supersaturated solid solution [13].

Here, U-6wt%Nb powders have been fabricated by a centrifugal atomization process [16,17] that leads to rapid solidification of the alloy particles. The objective of this work was to characterize the microstructures of the powder particles in order to assess the potential of the U-6wt%Nb rapidly solidified powder particles as the distributed fuel phase in dispersion-type nuclear fuels.

2. Materials and Methods

2.1. Materials fabrication

U-6wt%Nb (U-6Nb), or ~U-14at%Nb, powders were fabricated by a centrifugal atomization process [16,17] using 99% pure U and 99.8% pure Nb metal. A base pressure of 3×10^{-4} torr was obtained prior to pouring of the molten alloy. The feed rate of the molten alloy to the atomization chamber was ~50–100 g/s to a graphite atomization disk rotating at ~30000–40000 rpm. A cooling medium of high-purity (99.999%) Ar gas was used, and the atomized powder was passivated in the atomization chamber for 24 h in the high-purity Ar atmosphere during cooling. The powder was sieved by 50 μm and the powder size distribution was then measured with a dry particle size analyzer (laser diffraction).

2.2. Materials characterization

Powder specimens were prepared for optical metallography by affixing powder particles to carbon tape and polishing on 1-μm diamond paper to cross-section the particles. TEM specimens were prepared using a focused ion beam (FIB) lift-out method. FIB sample preparation was performed using an FEI Nova 600 Nanolab Dualbeam Focused Ion Beam Scanning Electron Microscope (FIB-SEM).

X-ray diffraction (XRD) experiments were conducted with an APD 3720 Philips XRD vertical goniometer using CuK_{α}radiation. SEM images were acquired in the FIB with an accelerating voltage of 5 kV. Transmission electron microscopy (TEM) was conducted on a Philips CM300 FEG ST TEM operating at an accelerating voltage of 300 kV. The TEM is equipped with a Gatan Imaging Filter (GIF) and an X-ray energy dispersive spectrometer (Oxford Instruments). Conventional TEM imaging and diffraction, annular dark-field scanning TEM (ADF-STEM) imaging, spectroscopic

energy-filtered TEM (EFTEM) imaging, and energy-dispersive spectrometry (EDS) were used to analyze the particles in the TEM.

3. Results

3.1. Particle Size Distribution and Morphology

The particle size distribution of the atomized powder is shown in Figure 1. This plot provides the overall distribution for the as-processed powder, as well as the distributions after the powder was sieved to separate particles that were <50 μm or >50μm. All three distributions are unimodal, narrow, and skewed to larger particle sizes. The mean particle size of the as-processed powder particles was ~65–70 (±25) μm, with a median and mode of ~65 μm and ~45 μm, respectively. The statistics for all three distributions are provided in Table 1. The particle size has been found to be a function of multiple processing variables during centrifugal atomization, including the frequency of the rotating disk, the disk diameter, the melt feed rate, surface tension, and the density of the molten alloy [17].

Figure 2 presents SEM images of the as-processed U-6Nb powder, showing that the particles produced by the centrifugal atomization process are spherical with smooth surfaces. The spherical shape of the particles, while dependent on the size of the liquid alloy droplet [18] and therefore on the variables mentioned above, is mainly a function of the surface tension of the droplet [16,17] and the thermal conductivity of the rotating disk material [16,19], with more spherical particle shapes resulting from disk materials with higher thermal conductivities [19]. As seen in the SEM images in Figure 2, the particles are spherical from sizes of ~50 μm (center image) down to ~8 μm (right image). Particle shapes that deviated from spherical were typically observed when the particle size exceeded ~50–60 μm.

3.2. Particle Microstructure

3.2.1. Surface Oxide Layer

A surface oxide layer was detected on the rapidly solidified U-6Nb powder particles. The presence of the oxide layer is revealed in the EFTEM images of Figure 3(a), which shows a zero-loss image of the surface region of a U-6Nb powder particle with a corresponding oxygen map. The oxygen elemental map was acquired using the three-window technique [20,21] with the oxygen K edge (532 eV). The images in Figure 3(a) were recorded with the alloy-oxide interface edge-on relative to the electron beam (i.e., parallel to the

electron beam). Compositional analysis of the oxide layer using EDS measured (in at.%) ~64(±7)% O, 36(±4)% U, with no detectable levels of Nb.

Figure 3(b) shows dark-field TEM images of the surface oxide layer. These images were obtained after orienting the U-6Nb powder particle along the [110] zone axis, as indicated in the inset diffraction pattern in Figure 3(b). (This [110] zone axis corresponds to the bcc γ phase of the U-6Nb alloy, though the weak reflections in the diffraction pattern are indicative of metastable phase formation, which will be discussed subsequently.) The inset diffraction pattern reveals that there is not a preferred crystallographic orientation relationship between the examined oxide layer and the underlying alloy particle. The dark-field images were acquired using the Bragg reflections that are highlighted by the boxes in the inset diffraction pattern (the left and right boxes correspond to the left and right images in Figure 3(b), respectively). Each of these highlighted Bragg reflections is in a systematic row condition, and the arrows in the figure are parallel to these systematic rows, showing that the two highlighted reflections are from different grains and the oxide layer is polycrystalline. The images in Figure 3 also show that the oxide surface layer is ~30–35 nm thick.

Figure 3(c) presents selected-area diffraction patterns acquired from the surface oxide grain that is shown in the right image of Figure 3(b), along with overlaid simulated diffraction patterns for UO_2 (assumed based on EDS measurements and inspection of the diffraction patterns) in the $[111]_{UO_2}$ and $[211]_{UO_2}$ zone axes, as indicated. The diffraction rings correspond to Pt, present as a protective layer deposited in the FIB during sample preparation. Based on the combined electron diffraction and EDS measurements, the surface oxide layer consists of the fcc UO_2 phase (space group $Fm\bar{3}m$ with lattice parameter $a_0 = 5.47$ Å).

3.2.2. Phase Morphology and Chemical Distribution

An experimental X-ray diffraction pattern acquired from the as-processed U-6Nb powder over the angular range $30° < 2\theta < 80°$ is shown in Figure 4. The calculated positions of diffraction peaks for the metastable bcc γ, orthorhombic α′, and monoclinic α″ phases are given directly beneath the experimental data. The major diffraction peaks in the experimental pattern correspond to the high-temperature bcc γ solid solution, as labeled in the figure. The arrows in Figure 4 indicate weak diffraction peaks in the experimental data. As shown in the figure, these weak diffraction peaks could be produced by the α′ or

α″ phases. The α′ phase is essentially a distorted version of the equilibrium orthorhombic α phase but supersaturated with Nb solute, causing lattice parameter variations manifested mainly by a contraction of the *b* axis of the unit cell. The α″ phase is characterized by a more sizeable contraction of the *b* axis accompanied by an increase of the angle *γ* between the *a* and *b* axes to slightly greater than 90°, producing a monoclinic structure. Both metastable phases are the result of a martensitic transformation from the high-temperature γ phase [11,14,22,23]. The α′ and α″ phases are typically differentiated in X-ray diffraction data by the peak splitting of certain (*hkl*) reflections that indicate monoclinic α″ phase formation [11]. This peak splitting is caused by the increased angle γ in the monoclinic structure relative to the orthorhombic structure, evidenced in the angular range of these experiments by the splitting of the (111) (2θ ~ 39.5°) and (131) (2θ ~ 61.0°) reflections into the (111)–($\bar{1}$11) and (131)–($\bar{1}$31) doublets, respectively, as indicated in the calculated diffraction peaks in Figure 4. The overall signal-to-noise ratio of the experimental diffraction data combined with the low intensity of these peaks complicates assignment of these weak peaks to either the α′ or α″ phase. The low intensity of these peaks is likely a result of quench-induced strain produced by extreme thermal gradients during the rapid solidification process [13].

The optical micrographs in Figure 5 reveal a dendritic microstructure. This dendritic structure likely results from Nb segregation during rapid solidification of the alloy particles and is present in all of the examined U-6Nb particles regardless of particle size. Similar microstructures have been observed in atomized U-Mo powders [16,17].

TEM was conducted to further assess the phases, morphology, and composition of selected powder particles. It should be noted that grain boundaries were not observed, in either optical or TEM analyses, in any of the examined particles. Figure 6(a) shows an ADF-STEM image of a cross-section taken from a particle with a diameter of ~10 μm. The surface of the particle is indicated in the image, and the dendritic structure observed in the optical micrographs in Figure 5 is clearly evident in the ADF image, revealing that these dendrites extend radially through the spherical particle. The contrast in the ADF image, while potentially exhibiting a dependence on atomic number, Z, [24], represents a convolution of the effects of mass-thickness, strain, and diffraction conditions with this Z-contrast. The distribution of uranium and niobium were mapped using EDS. The region of acquisition of the chemical maps is indicated by the box in Figure 6(a), and Figure

6(b) shows an ADF-STEM image of this region with the corresponding overlaid uranium and niobium maps. The EDS maps were acquired using the U-L_α and Nb-L_α characteristic X-ray lines. The EDS map shows uranium enrichment in the dendrites with niobium segregated to the regions between dendrites. The arrow in Figure 6(b) points to an interdendritic region where the contrast shows a discernible composition variation between dendrites. This dendritic growth and compositional segregation will be discussed subsequently.

Figure 7(a) shows an ADF-STEM image of a cross-section removed from another larger (~40 μm in diameter) U-6Nb particle. Here, the orientation of the specimen and imaging conditions were set to allow imaging of the twinned domain structure that is present in the interdendritic regions of all particles that were examined. The image was acquired with the electron-beam direction approximately parallel to the [100] zone axis of the specimen, as indicated in the figure. The average composition in this twinned region, measured from 20 independent EDS spectra using the U-L_α and Nb-K_α characteristic peaks [25], was ~7wt%Nb, 93wt%U, approximately the nominal composition of the alloy. Preliminary EDS measurements across the dendrites indicate an increase in the Nb content at the edges of dendrites to as much as ~8–10wt%Nb and a sharp decrease at the center of primary dendrite arms to ~3–4wt%Nb. Figure 7(b) presents selected-area diffraction patterns acquired from this interdendritic region shown in Figure 7(a) in the [100], [110], and [311] zone axis, as indicated in the figure. The diffraction patterns reveal the twinned structure as the metastable cubic γ^0 phase. The γ^0 phase is a distortion of the bcc γ solid solution due to displacement of the body-centered atoms in adjacent bcc unit cells in opposite <100> directions [26,27]. The weak reflections in the diffraction patterns result from the atom displacements. All diffraction patterns in Figure 7(b) are indexed for both the metastable γ^0 and bcc γ parent phase to illustrate the crystallographic relationship between the two structures.

4. Discussion

During atomization processes, solidification typically initiates heterogeneously during flight of the molten, spherical particles [28]. The undercooling is inversely proportional to the size of the liquid droplet, and sufficiently high undercoolings for homogeneous nucleation are generally not achieved unless the particle size is extremely small [28,29].

This size effect is largely due to the size-dependent surface tension of the liquid alloy droplet, as the liquid-vapor interface energy is a function of the droplet diameter when the interface is curved. It has been suggested that changes to the liquid-vapor interface energy are negligible until the droplet diameter is less than ~100 nm [30-32], though solidification rates consistent with homogeneous nucleation have been observed in liquid droplets with diameters of 2–8 μm [33]. Attainment of these high undercoolings is further inhibited by the presence of heterogeneities such as inclusions and surface oxidation processes, and the level of catalyzed solidification is dependent on the size and chemistry of the heterogeneity [28,33,34]. Though it cannot be stated conclusively whether the oxide layer on the surfaces of the U-6Nb particles formed during or after the atomization process, there was no evidence of nucleation in particle interiors in all observed particles. Rather, based on the observed morphologies of the dendritic microstructure (Figure 5) and the surface oxide layer (Figure 3), nucleation likely initiated heterogeneously at the surfaces of particles, potentially at sites where a surface oxide was present.

As a result of the atomization process, large undercoolings develop in the molten particles and the rapid quench rates from the liquid to room temperature produce extremely high solidification front velocities. Solidification front velocities can reach values >1 m/s due to the large surface-to-volume ratio of particles and high convective heat flux (up to ~10^6 K/s) from the molten particle to the atomizing gas [28], which can result in severe microstructural refinement, extension of solute solubility limits, non-equilibrium phase formation, and even partitionless solidification. These high velocities lead to deviations from local equilibrium at the solid-liquid interface, and the equilibrium phase diagram is no longer applicable as a guide to phase formation. For example, the U-Nb equilibrium phase diagram [15] indicates that for a U-6Nb alloy, the first phase to form upon cooling from the liquid would be the bcc γ solid solution with an approximate composition of U-11wt%Nb. Clearly there was a departure from equilibrium solidification conditions given the U-rich dendrite formation shown in Figure 6 and the measured compositions across dendrites and in the interdendritic regions (approximately the nominal composition of the alloy). Metastable phase formation is therefore expected due to the rapid solidification process (RSP).

Based on the micrographs in Figures 5–7, dendritic growth initiated at particle surfaces and progressed radially inward, opposite the direction of heat flow along the

positive thermal gradient. Dendrite formation indicates a morphologically unstable solid-liquid interface during rapid solidification. This morphological instability is the result of Nb rejection from the alloy as solidification progresses, leading to Nb enrichment in a constitutionally undercooled boundary layer ahead of the solid-liquid interface. This solute rejection allows local perturbations along the solid-liquid interface to amplify and extend into the undercooled liquid, and growth proceeds as these perturbations grow and advance the solidification front with dendritic growth. As these new undercooling-induced perturbations amplify, cusps and troughs develop and grow. Unlike at troughs, solute can be rejected laterally at the peaks of the perturbations, resulting in an increased undercooling and growth rate at the peaks [35]. The excess solute accumulated in the perturbation troughs can lead to the formation of secondary dendrite arms. This solute rejection during dendritic growth in the U-6Nb particles is displayed in the elemental map of Figure 6. The dendrites are U-rich relative to the overall microstructure, and as they solidify Nb is rejected into the liquid. The Nb-rich boundary layer is indicated by the arrow in Figure 6(b), where a contrast variation across the inderdendritic region is evident in the ADF image. The Nb-rich layer exhibits dark contrast in this image, and it is evident in both the contrast of the ADF image and shading of the elemental map of Figure 6(b) that a region of increased uranium content (though lower than the U-rich dendrites) is present between the Nb "sheath" layers of the bounding dendrites. These high-uranium-content regions correspond to the twinned, γ^0 metastable structure shown in Figure 7.

The primary and secondary arm spacings of dendrites depend on the product of the thermal gradient and solidification front velocity, and the scale of the microstructure typically remains constant during conventional solidification processes [35]. However, Figures 5–7 show that the structure in the U-6Nb particles displays a degenerate dendritic solidification mode, where secondary dendrite arms are either difficult to distinguish, suppressed in regions, or nonexistent. This is common in the presence of large undercoolings and high solidification rates [28], where the solid-liquid interface velocity approaches or exceeds the solute interface diffusion rate [35] and the velocity-dependent partition coefficient deviates significantly from its equilibrium value [36,37]. This deviation in partitioning during rapid solidification is evident in the measured composition in interdendritic regions with the twinned γ^0 structure (indicated by the arrow in Figure 6(b)), ~7wt%Nb, the nominal composition of the alloy. In these

interdendritic regions, a large driving force for solidification will develop due to the imposed undercooling, eventually leading to diffusionless solidification at the compositions that are present in these regions. Figure 6 also shows that in this particular U-6Nb particle, dendritic growth ceased ~5–6 μm beneath the surface and the growth mode transitioned to a structure, based on the contrast in the ADF image, consistent with partitionless solidification or complete solute trapping [36,37]. This region at the center of the particle where non-dendritic growth occurred consists of the same twinned γ^0 structure with the nominal alloy composition, as observed in interdendritic regions. This implies an accelerating solid-liquid interface during solidification, with the solidification front reaching the absolute stability limit [35,38,39]. It should be noted that this transition to partitionless solidification was not present in the particle shown in Figure 7, and the twinned γ^0 structure with the nominal alloy composition was present only in interdendritic regions. This transition is dependent on solidification rate and hence particle size (the diameter of the particle in Figure 6 was ~10 μm while the diameter of the particle in Figure 7 was ~40 μm). The heat extraction rates, thermal gradients, and solidification rates experienced by the particles will be a function of particle size, and hence, even with the relatively narrow particle size distribution shown in Figure 1, it is difficult to assess correlations between the observed microstructures and the solidification conditions without examination of a large number of individual particles. Trends in the microstructure, composition, and crystallography with particle size is the focus of ongoing work.

As discussed, the observed microstructures in the centrifugally atomized U-6Nb powder particles are a result of a RSP, where a large undercooling in the U-Nb melt yields a high solidification front velocity [35]. While the observed dendritic morphology and measured compositions are indicative of a RSP, the crystallographic phases in the particles can be discussed in terms of metastable phase formation as a function of composition, as observed in quenching experiments [11,22,23,27] from the high-temperature bcc γ solid solution. The XRD data in Figure 4 indicates a predominantly bcc γ structure with weak reflections that potentially correspond to metastable α′ or α″ phase formation. Combining this XRD data with the TEM observations of Figure 6 and 7 suggests that the strong diffraction peaks in Figure 4 corresponding to the γ structure result from the metastable twinned $\tilde{\gamma}$ phase in interdendritic regions and the weak

reflections corresponding to the metastable α′ or α″ phases are produced by the dendritic microstructure. The ability to differentiate between the γ and γ^0 phases and α′ and α″ phases in the XRD data is complicated by the low intensity of diffraction peaks other than those that correspond to the parent γ phase in interdendritic regions. This is likely due to a low volume fraction of dendrites relative to interdendritic phases (or partitionless regions, which, as discussed previously, is dependent on particle size), low signal-to-noise ratio of the experimental diffraction data, and quench-induced strains produced by the RSP [13].

The transformation sequence of metastable phases from the high-temperature γ-related phases to the low-temperature α-related phases is given by $\gamma \rightarrow \gamma^0 \rightarrow (\gamma^0_d)^{\dagger} \rightarrow \alpha'' \rightarrow \alpha'$ [26]and the phase transitions consist primarily of successively greater shears of $\{112\}_\gamma$ planes in $<111>_\gamma$ directions followed by a shuffling of atoms along the [100] direction of the γ phase [11,27,40]These metastable phases form even at relatively low cooling rates due to sluggish kinetics [13] and can therefore be expected to form during the rapid solidification and quench rates experienced by the U-6Nb powder particles during centrifugal atomization processing. Approximate composition ranges for the formation of these metastable phases have been determined in prior studies [11,22,23,27]. Over the relevant composition ranges in this study, the α′ phase forms at compositions up to ~3–4wt%Nb, the α″ phase forms at compositions between ~3–4wt%Nb and ~7wt%Nb, and the γ^0 phase forms at compositions beyond ~7wt%Nb. It should be noted that the nominal composition of the U-6Nb alloy and the measured composition in the interdendritic regions is close to the intermediate composition where the transition between γ^0 and α″ occurs, and γ^0 is believed to be a precursor to the martensitic α″ phase [27].

The majority of the structure of the U-6Nb powder particles, based on the contrast in the optical micrographs of Figure 5 and the TEM images and diffraction patterns of Figures 7, is the γ^0 phase. The γ^0 phase is a cubic phase, based on the bcc γ solid solution, with space group $I\bar{4}3m$ [26]. The lattice parameter of the γ^0 phase is approximately twice

---

† The γ^0_d phase forms upon low-temperature aging of the γ^0 phase. This phase is tetragonal with space group P4/nmm and lattice parameters $a = \sqrt{2}a_\gamma$ and $c = a_\gamma$ [26]. The γ^0_d phase was not observed in this study.

that of the γ phase, and the structure is described by eight γ unit cells with correlated displacements of body-centered atoms along <100> directions. (The γ^0_d phase mentioned above in the phase transformation sequence is characterized by further correlated shifts of body-centered atoms along a specific <001> direction.) As there is equal statistical probability of the body-centered atoms moving along [100], [010], or [001] directions in the γ^0 structure, the identities of sublattices may be lost over distances comparable to the correlation distances of the displacements, resulting in antiphase domains with <1/4,1/4,1/4> shifts between unit cell origins of the domains. XRD data has shown that these atomic displacements are correlated over a distance of ~5 nm [26]. The selected-area diffraction patterns shown in Figure 7 confirm that the twinned structure in interdendritic regions is the γ^0 phase, and the measured composition of this phase (~7wt%Nb) agrees with the expected composition range for γ^0 phase formation [11,22,23,27].

Prior studies [14,27,41] indicate that the twinning in γ^0 consists of multiple lamellar domains that are twin-related about $\{110\}_\gamma$ planes. The crystallographic nature of the twinned structure shown in Figure 7, as well as any crystallographic relationship between the interdendritic γ^0 and the dendritic α-related phases, is still being investigated and will be the focus of future work. The specific α-related phase present in dendritic regions is also under examination, and preliminary EDS measurements in the U-rich dendrites indicate a composition approximately at the transition between α′ and α″ [11,22,23,27].

Lastly, given the observed microstructures in the U-6Nb particles, what are the implications for use of the powder in dispersion-type nuclear fuel applications? As mentioned previously, U-6Nb alloys possess the greatest corrosion resistance and mechanical properties when quenched at high enough rates to obtain the metastable martensitic α″ phase. While the cubic γ^0 phase can potentially provide improved dimensional stability relative to the equilibrium orthorhombic α phase, the presence of adjacent α-related dendrites can deteriorate the corrosion resistance. This two-phase (or even multi-phase if it is determined that more than one α-related phase is present) structure with varying Nb content can lead to microscopic anodic and cathodic regions in the particles [13], reducing the corrosion properties of the alloy. Post-processing solution treatment at a temperature in the γ-phase field followed by rapid quenching at a sufficient

rate (>20 K/s [13]) to produce single-phase, fully martensitic α″ particles can potentially yield powders with the desired properties for dispersion-type nuclear fuels.

5. Conclusions

U-6wt%Nb powders were produced by a centrifugal atomization process. The morphology and microstructure of the particles were characterized to assess the potential of the rapidly solidified powder particles as a distributed fuel phase in dispersion-type nuclear fuels. The main conclusions can be summarized as:

1. The powder particles were spherical with a narrow size distribution achieved by appropriate sieving. The mean particle size of the as-processed powder particles was ~65–70 (±25) μm.
2. An ~30–35-nm-thick UO_2 surface oxide layer was detected on the particles.
3. Based on combined XRD, metallography, and TEM data, the microstructure of the U-6Nb particles consists of a dendritic structure formed during rapid solidification. The dendrites are comprised of a metastable α-related phase and interdendritic regions consist of the metastable γ^0 phase. These interdendritic γ^0 regions are highly twinned.

The crystallography of the observed twinning, crystallographic relationship between the interdendritic γ^0 and the dendritic α-related phases, and specific nature of the α-related phase present in dendritic regions is the focus of ongoing work.

Acknowledgments

This work was performed under the auspices of the U.S. Department of Energy by Lawrence Livermore National Laboratory (LLNL) under Contract No. DE-AC52-07NA27344. Work was funded by the Laboratory Directed Research and Development Program at LLNL under project tracking code 13-SI-002.

The authors at LLNL would like to acknowledge the support of Jackson Go for metallographic work, Cheng Saw for X-ray diffraction measurements, Nick Teslich for FIB specimen preparation, and Mark Wall for metallographic and X-ray diffraction specimen preparation. The authors at KAERI would like to acknowledge the support of Se Jung Jang and Eung Soo Kim for atomization, Jong Hwan Kim for particle size analysis, Hyun Seok Ahn for sieving and chemical analysis, and Jung Do Kim for international transport preparation and licensing.

References

[1] International Atomic Energy Agency, Development status of metallic, dispersion and non-oxide advanced and alternative fuels for power and research reactors, IAEA-TECDOC-1374 (2003).
[2] M.A. Pouchon, M. Nakamura, C. Hellwig, F. Ingold, and C. Degueldre, J. Nucl. Mater. 319 (2003) 37.
[3] A.M. Savchenko, A.V. Vatulin, A.V. Morozov, V.L. Sirotin, I.V. Dobrikova, G.V. Kulakov, S.A. Ershov, V.P. Kostomarov, and Y.I. Stelyuk, J. Nucl. Mater. 352 (2006) 372.
[4] A.M. Savchenko, A.V. Vatulin, A.V. Morozov, I.V. Dobrikova, S.A. Ershov, S.V. Maranchak, Z.N. Petrova, and Y.V. Konovalov, J. Nucl. Mater. 352 (2006) 334.
[5] A. Savchenko, I. Konovalov, A. Vatulin, A. Morozov, V. Orlov, O. Uferov, S. Ershov, A. Laushkin, G. Kulakov, S. Maranchak, and Z. Petrova, J. Nucl. Mater. 362 (2007) 356.
[6] A.M. Savchenko, A.V. Vatulin, E.M. Glagovsky, I.I. Konovalov, A.V. Morozov, A.V. Kozlov, S.A. Ershov, V.A. Mishunin, G.V. Kulakov, V.I. Sorokin, A.P. Simonov, Z.N. Petrova, and V.V. Fedotov, J. Nucl. Mater. 396 (2010) 26.
[7] V.P. Sinha, P.V. Hegde, G.J. Prasad, S. Pal, and G.P. Mishra, J. Nucl. Mater. 427 (2012) 12.
[8] K.A. Terrani, J.O. Kiggans, and L.L. Snead, J. Nucl. Mater. 427 (2012) 79.
[9] A.N. Holden, *Physical Metallurgy of Uranium*, Reading, MA: Addison-Wesley, 1958.
[10] G. Lagerberg, J. Nucl. Mater. 9 (1963) 261.
[11] K. Tangri, and D.K. Chaudhuri, J. Nucl. Mater. 15 (1965) 278.
[12] K.H. Eckelmeyer, Diffusional transformations, strengthening mechanisms, and mechanical properties of uranium alloys, Sandia National Laboratories Report SAND 82-0524 (1982).
[13] K.H. Eckelmeyer, A.D. Romig, and L.J. Weirick, Metall. Trans. A 15 (1984) 1319.
[14] R.D. Field, and D.J. Thoma, J. Nucl. Mater. 436 (2013) 105.
[15] T.B. Massalski, *Binary Alloy Phase Diagrams*, ASM, Materials Park, OH (1990).
[16] K.-H. Kim, D.-B. Lee, C.-K. Kim, G.E. Hofman, and K.-W. Paik, J. Nucl. Mater. 245 (1997) 179.
[17] C.-K. Kim, J.-M. Park, and H.-J. Ryu, Nucl. Eng. Technol. 39 (2007) 617.
[18] O.S. Nichiporenki, A.G. Tsipunov, and Y.F. Ternovi, Poroshk. Metall. 253 (1984) 1.
[19] T. Kato, and K. Kusaka, Mater. Trans. JIM 31 (1990) 363.
[20] C. Jeanguillaume, P. Trebbia, and C. Colliex, Ultramicroscopy 3 (1978) 237.
[21] R.F. Egerton, *Electron Energy-Loss Spectroscopy in the Transmission Electron Microscope* New York: Plenum Press, 1996.
[22] M. Anagnostidis, M. Colombié, and H. Monti, J. Nucl. Mater. 11 (1964) 67.
[23] R.A. Vandermeer, Acta Metall. 28 (1980) 383.
[24] S.J. Pennycook, Ultramicroscopy 30 (1989) 58.
[25] A.D. Romig, J. Microsc. 135 (1984) 191.
[26] H.L. Yakel, J. Nucl. Mater. 33 (1969) 286.
[27] R.D. Field, D.J. Thoma, P.S. Dunn, D.W. Brown, and C.M. Cady, Phil. Mag. A 81 (2001) 1691.
[28] E.J. Lavernia, and T.S. Srivatsan, J. Mater. Sci. 45 (2010) 287.
[29] R.F. Cochrane, P.V. Evans, and A.L. Greer, Mater. Sci. Eng. 98 (1988) 99.
[30] J.A.V. Butler, Proc. R. Soc. Lond. A 135 (1932).
[31] E.A. Guggenheim, Trans. Faraday Soc. 35 (1940) 397.
[32] L. Liu, T.H. Wang, J.C. Li, and Q. Kiang, Sol. State Comm. 152 (2012) 573.
[33] D. Turnbull, J. Chem. Phys. 20 (1952) 411.
[34] J.H. Perepezko, Mater. Sci. Eng. 65 (1984) 125.

[35] W. Kurz, and D.J. Fisher, *Fundamentals of Solidification*, Aedermannsdorf, Switzerland: Trans Tech Publications, 1992.
[36] J.C. Baker, and J.W. Cahn, Acta Metall. 17 (1969) 575.
[37] M.J. Aziz, and T. Kaplan, Acta Metall. 36 (1988) 2335.
[38] W.W. Mullins, and R.F. Sekerka, J. Appl. Phys. 35 (1964) 444.
[39] S.R. Coriell, and R.F. Sekerka, J. Cryst. Growth 61 (1983) 499.
[40] K. Tangri, and G.I. Williams, J. Nucl. Mater. 4 (1961) 226.
[41] B.A. Hatt, J. Nucl. Mater. 19 (1966) 133.

Table

Table 1. Statistics of particle size distribution for U-6Nb powder.

	Mode (µm)	**Median (µm)**	**Mean (µm)**	**σ (µm)**
As-processed	45–50	60–65	65–70	25
<50 µm	30–35	35–40	40–45	15
>50 µm	50–55	60–65	65–70	20

Figures

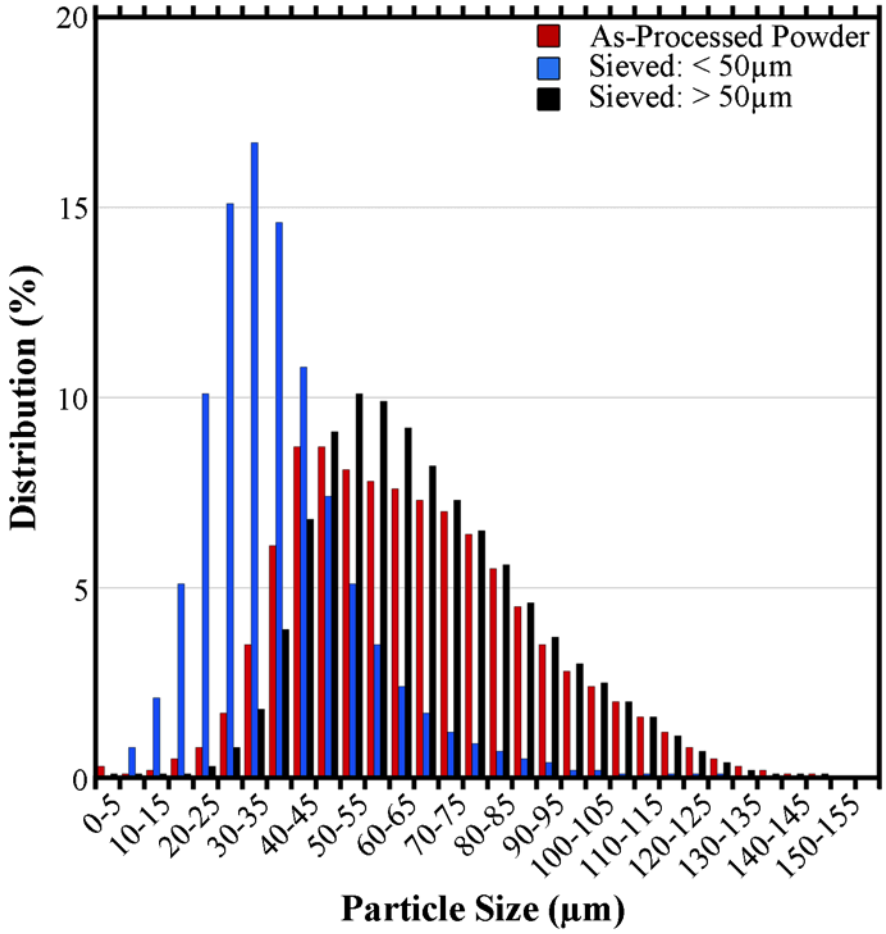

Figure 1. Size distribution of the atomized U-6Nb powder. The histogram shows the distribution of the as-processed powder, as well as the distributions after sieving the powder for sizes <50 µm and >50µm.

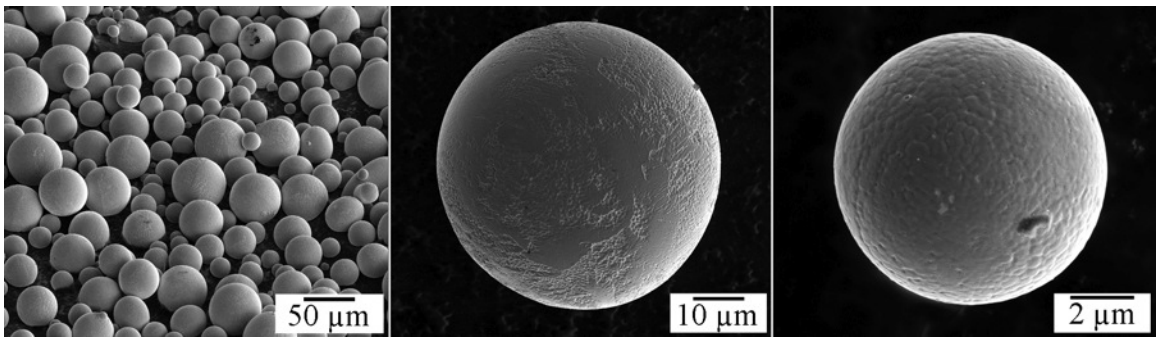

Figure 2. SEM images of the as-processed U-6Nb powder particles.

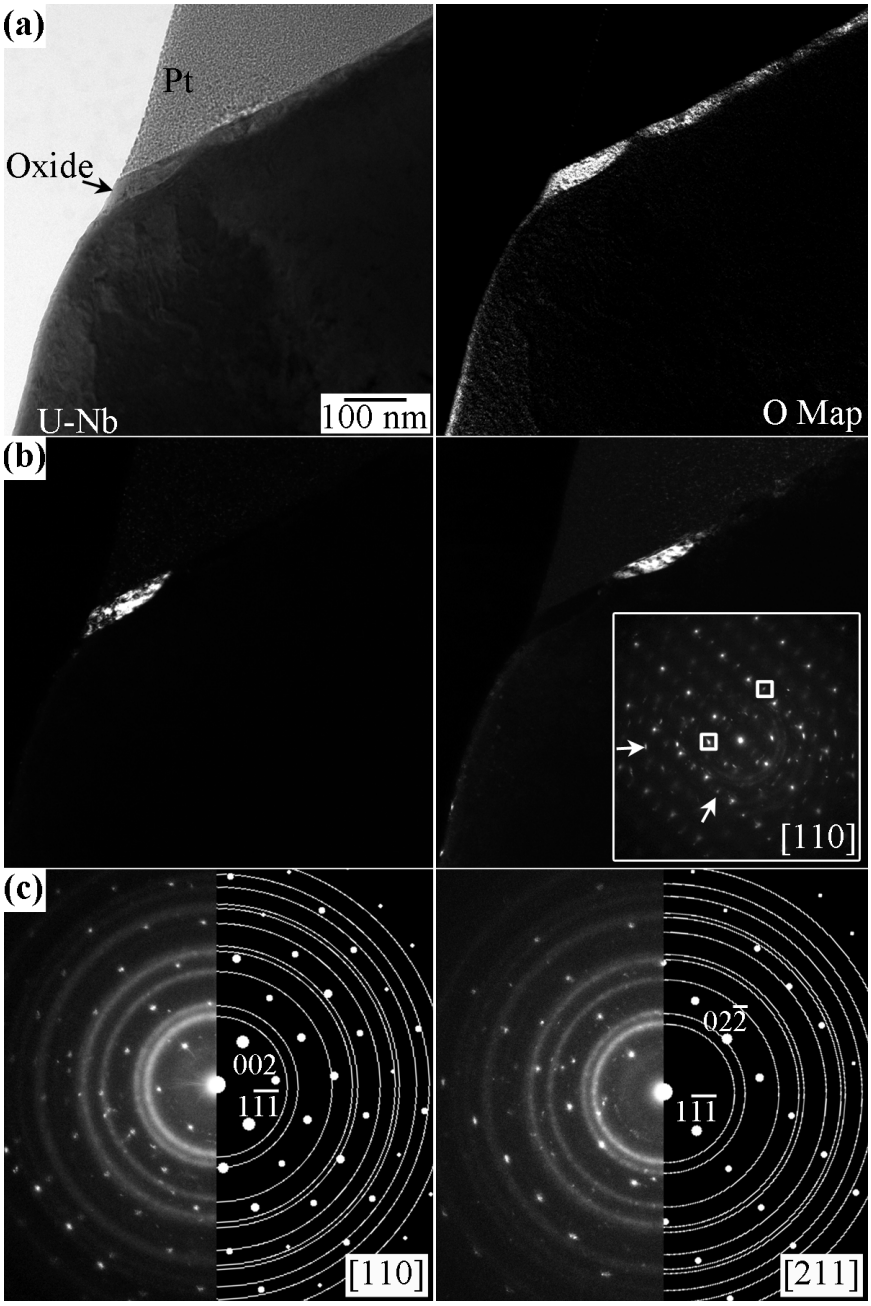

Figure 3. (a) EFTEM images of the surface of a U-6Nb particle showing (left) a zero-loss image and (right) an oxygen map, which reveals the surface oxide layer. (b) Dark-field TEM images of the oxide layer using the Bragg reflections indicated by the boxes in the inset diffraction pattern (left/right boxes correspond to left/right images). (c) Experimental selected area diffraction patterns from the oxide layer overlaid with simulated diffraction patterns for UO_2 in a (left) [110] and (right) [211] zone-axis orientation. The Pt in the images, deposited as a protective layer during FIB sample preparation, produces the diffraction rings in (c).

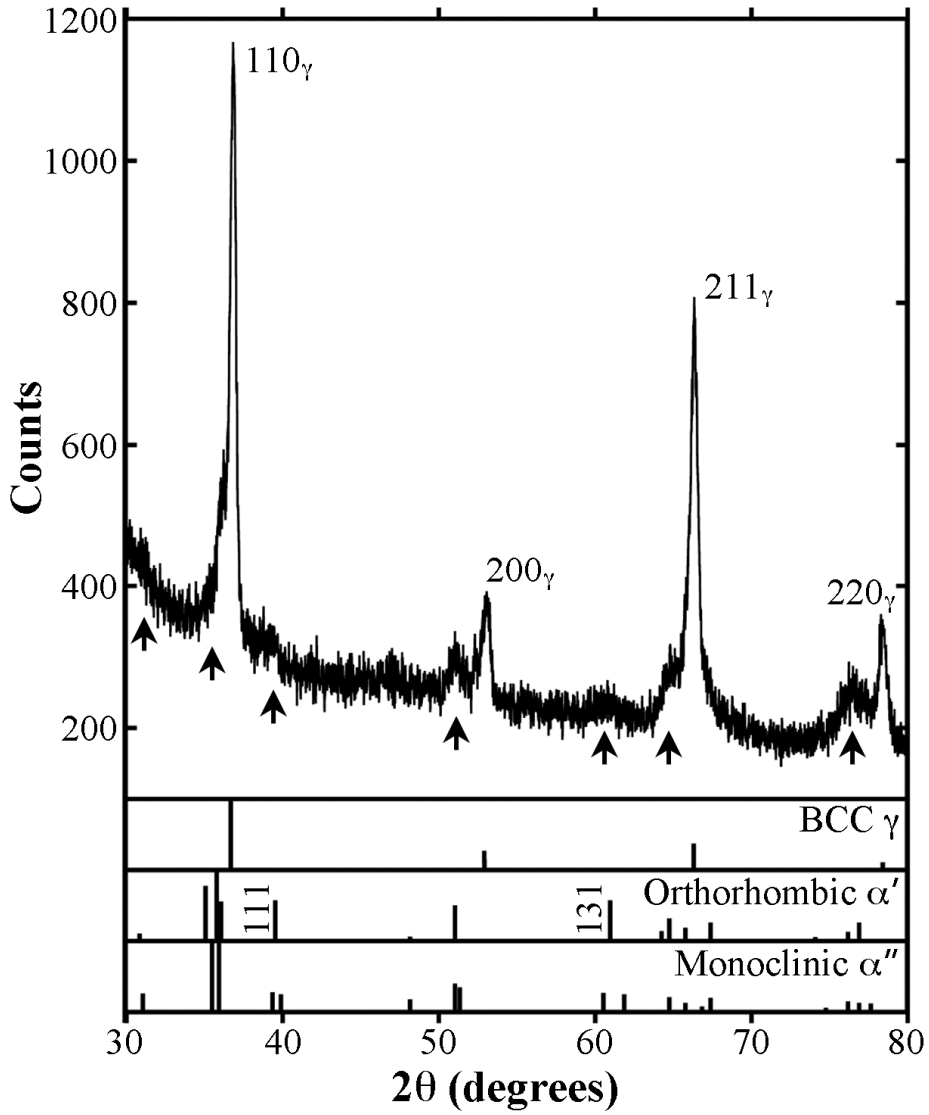

Figure 4. Experimental X-ray diffraction pattern acquired from the as-processed U-6Nb powder, with calculated positions of diffraction peaks for the bcc γ, orthorhombic α′, and monoclinic α″ phases.

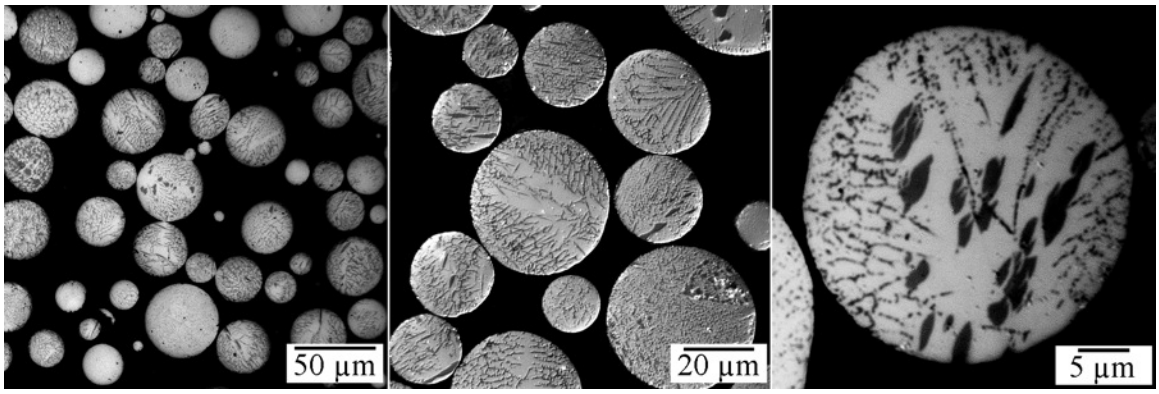

Figure 5: Optical micrographs of sectioned U-6Nb particles showing compositional segregation.

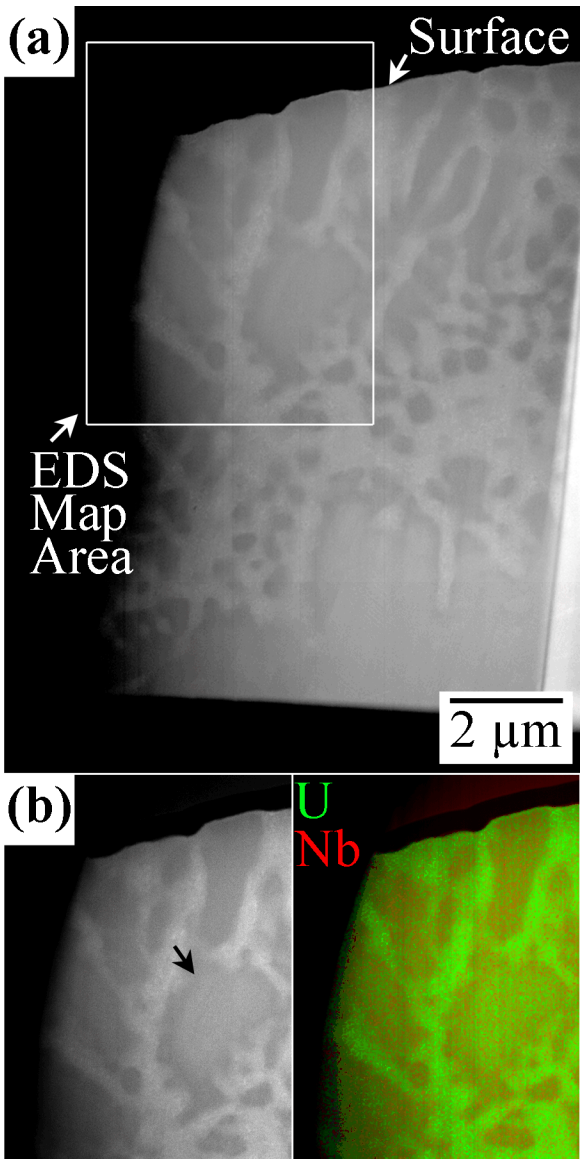

Figure 6. (a) ADF-STEM image showing cross-sectional view of a U-6Nb particle. The dendritic structure is evident in the image. The surface of the particle is indicated. (b) ADF-STEM image and corresponding EDS elemental map from the region indicated in (a), revealing the distribution of U (green) and Nb (red). The arrow in (b) indicates an interdendritic region where a composition variation is discernible between dendrites.

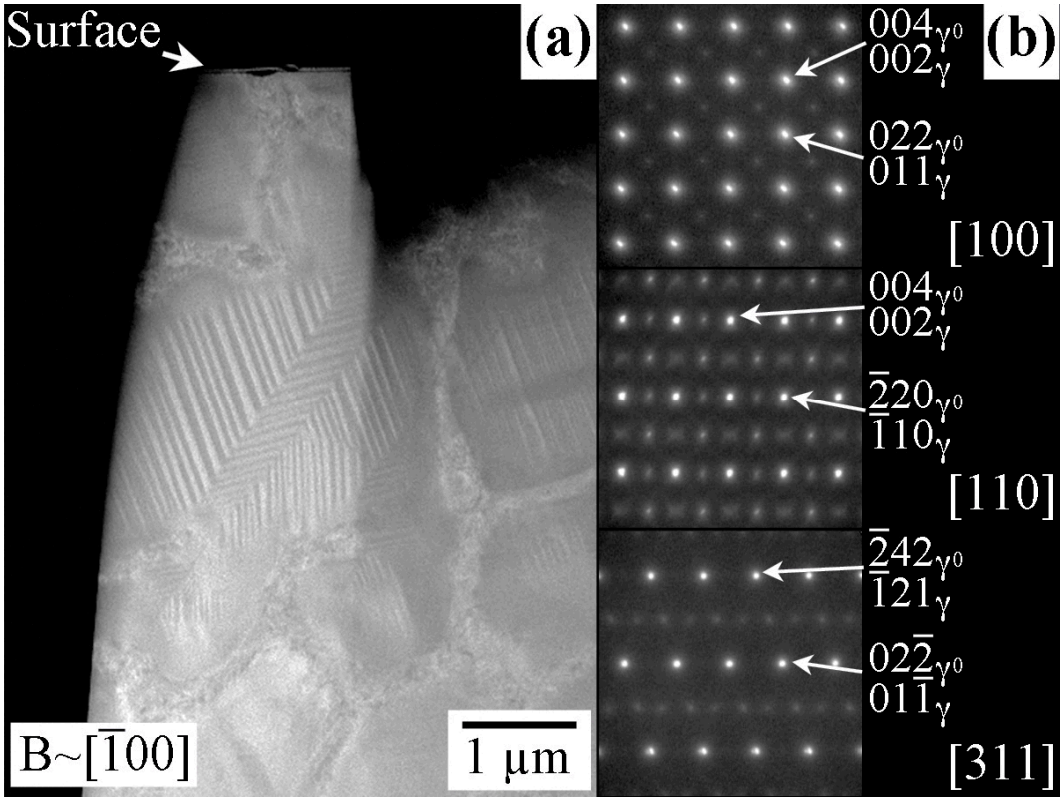

Figure 7. (a) ADF-STEM image revealing a twinned domain structure in the interdendritic region of a U-6Nb particle. The direction of the electron beam, B, is approximately parallel to the [$\bar{1}$00] zone axis of the specimen, as indicated. (b) Selected-area diffraction patterns from this interdendritic region in the [100], [110], and [311] zone axes. Indexing is provided for both the metastable γ^0 phase and the high-temperature bcc γ parent phase to illustrate the crystallographic relation between the two structures. The zone axes are the same for both structures.